A REVIEW OF OPTICAL F-REGION PROCESSES IN THE POLAR ATMOSPHERE

Jean-Claude Gérard

Institut d'Astrophysique - Université de Liège
B-4200 Liège, Belgium.

ABSTRACT

The importance of optical emissions is described in the context of the magnetosphere-ionosphere-neutral atmosphere interactions. Excitation processes of some important F-region emissions in the polar regions are reviewed. The importance of optical emissions for the determination of the quantum yields and quenching coefficients is illustrated for the $O^+(^2P)$, $O^+(^2D)$, $N(^2D)$, $N(^2P)$ and $O(^1D)$ states and a set of values deduced from recent experiments such as the Atmosphere Explorer satellites is given. The effects of transport by neutral winds and electromagnetic drifts on the morphology are also discussed and illustrated by recent model calculations for $N(^2D)$ horizontal transport.

1. INTRODUCTION

High latitude optical emissions result from the interaction of the magnetospheric plasma with the earth's neutral and ionized atmosphere. Although the initial energy source always originates in the precipitated energetic particles and E-field, many indirect excitation mechanisms enhanced by the primary precipitation make substantial contribution and occasionally dominate the production of optical radiation. Consequently, the task of untangling the excitation processes of a given emission is essential when the emission is used as a tool to probe the polar atmosphere.

The interaction of the primary particles with the atmosphere

C. S. Deehr and J. A. Holtet (eds.), Exploration of the Polar Upper Atmosphere, 175–187.

produces secondary electrons, enhances the local ion and electron densities and temperatures and generates neutral winds and composition changes in the thermosphere (figure 1) in a way formally similar to the EUV radiation. The optical emissions (box "airglow excitation rates") constitute one of the products of this complex system and result from 1) the electron ionization and excitation of neutral constituents, 2) the excitation of low energy levels by the high energy tail of thermal electrons, 3) the dissociative recombination of molecular ions and 4) energy-transfer processes from metastable species carrying excitation energy. The total energy released as optical radiation in a typical magnetospheric substorm is about 10% of the total energy deposited by particle precipitation (Rees, 1975).

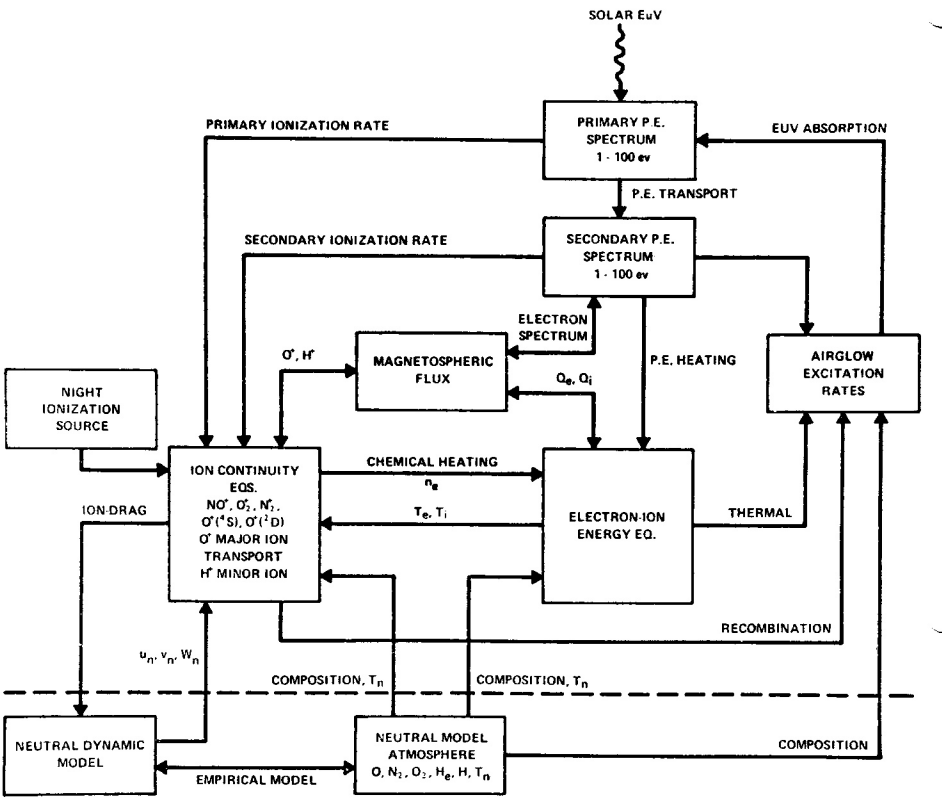

Figure 1 : Block diagram illustrating the magnetosphere-ionosphere-atmosphere interactions (from Roble 1975).

produces secondary electrons, enhances the local ion and electron densities and temperatures and generates neutral winds and composition changes in the thermosphere (figure 1) in a way formally similar to the EUV radiation. The optical emissions (box "airglow excitation rates") constitute one of the products of this complex system and result from 1) the electron ionization and excitation of neutral constituents, 2) the excitation of low energy levels by the high energy tail of thermal electrons, 3) the dissociative recombination of molecular ions and 4) energy-transfer processes from metastable species carrying excitation energy. The total energy released as optical radiation in a typical magnetospheric substorm is about 10% of the total energy deposited by particle precipitation (Rees, 1975).

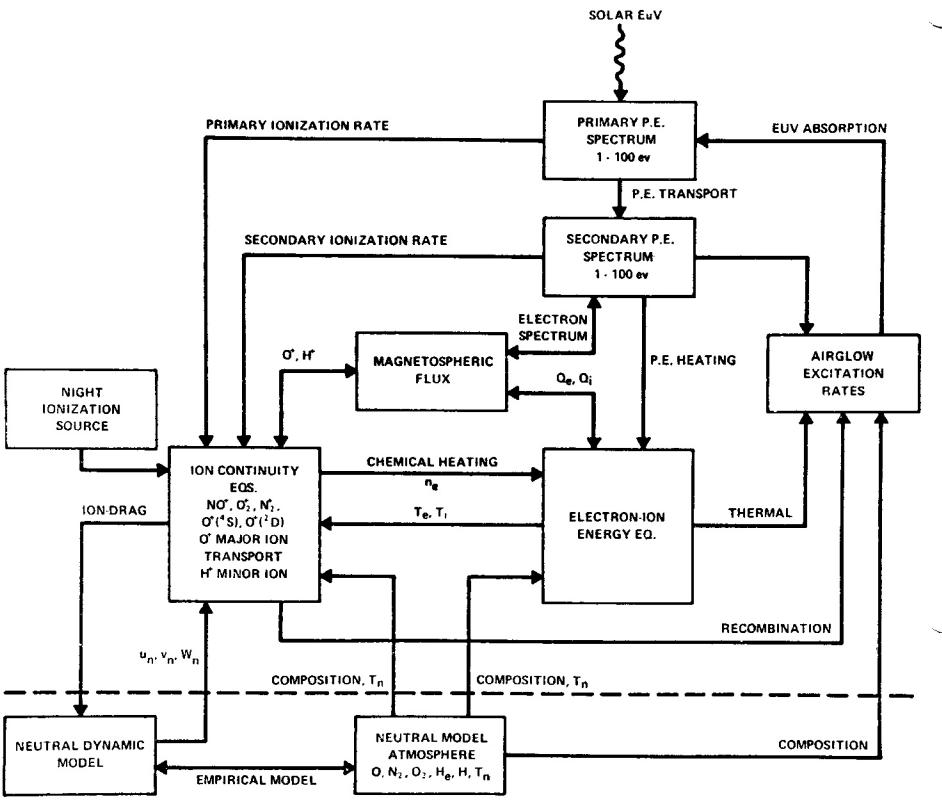

Figure 1 : Block diagram illustrating the magnetosphere-ionosphere-atmosphere interactions (from Roble 1975).

2. PRODUCTION AND QUENCHING OF F-REGION EMISSION

Spectroscopically, optical emissions fall into two categories: allowed transition having transition probabilities of the order of $10^8 s^{-1}$ and forbidden emissions arising from transition violating selection rules for electric dipoles. Corresponding transition probabilities range from more than 1 to less than $.10^{-5} s^{-1}$. The importance of forbidden transitions in this context is due to the fact that energy levels of atoms (or ions) lying a few electric volts above the ground state belong to the fundamental electronic configuration. Laporte's selection rule states that the parity of the total electronic angular momentum $1 = \Sigma 1_i$ must change during an electronic transition. Consequently, transition such as $NI\,^4S^o - {}^2D^o$ between states of same parity are forbidden. Other selection rules such as $\Delta S = 0$ and $\Delta L = \pm 1$ may also decrease the transition probability.

Quenching of metastable species X^n in the n state may proceed through one of the two paths:

$$X^n + M \rightarrow X^1 + M \qquad \text{(quenching)}$$

or

$$X^n + M \rightarrow Y + Z \qquad \text{(chemical reaction)}$$

In the former case, M is a second body not altered by the process, whereas in the latter, an actual chemical reaction involves the second body. In a steady state, the production and loss rates of X^n are equal and given by:

$$P_n = \left(\sum_1 A_{n,1} + \sum_i k_i [M_i]\right) [X^n] = \tau_e^{-1} [X^n],$$

where P_n is the volume production rate of X^n, $A_{n,1}$ the probability of the $n \rightarrow 1$ transition, k_i the deactivation coefficients and $\tau_e = \left(\sum_1 A_{n,1} + \sum_i k_i [M_i]\right)^{-1}$ is the effective lifetime. The volume emission rate $n \rightarrow m$ is thus given by:

$$\eta_{n,m} = [X^n] A_{n,m} = \frac{P_n}{B^{-1} + A_{n,m}^{-1} \sum_i k_i [M_i]}$$

where $B = \dfrac{A_{n,m}}{\sum_1 A_{n,1}}$ is the radiative branching ratio.

The effective lifetime at the peak of the emission rate profile may be considerably smaller than the radiative lifetime as will be shown below. Recent measurements (Deans and Shepherd 1978, Rees et al., 1977, Rusch and Gérard, 1980) have indicated

2. PRODUCTION AND QUENCHING OF F-REGION EMISSION

Spectroscopically, optical emissions fall into two categories: allowed transition having transition probabilities of the order of $10^{8}s^{-1}$ and forbidden emissions arising from transition violating selection rules for electric dipoles. Corresponding transition probabilities range from more than 1 to less than $.10^{-5}s^{-1}$. The importance of forbidden transitions in this context is due to the fact that energy levels of atoms (or ions) lying a few electric volts above the ground state belong to the fundamental electronic configuration. Laporte's selection rule states that the parity of the total electronic angular momentum $1 = \Sigma_i l_i$ must change during an electronic transition. Consequently, transition such as $NI\,^4S^o - {}^2D^o$ between states of same parity are forbidden. Other selection rules such as $\Delta S = 0$ and $\Delta L = \pm 1$ may also decrease the transition probability.

Quenching of metastable species X^n in the n state may proceed through one of the two paths:

$$X^n + M \rightarrow X^1 + M \qquad \text{(quenching)}$$

or

$$X^n + M \rightarrow Y + Z \qquad \text{(chemical reaction)}$$

In the former case, M is a second body not altered by the process, whereas in the latter, an actual chemical reaction involves the second body. In a steady state, the production and loss rates of X^n are equal and given by:

$$P_n = \left(\sum_1 A_{n,1} + \sum_i k_i [M_i]\right) [X^n] = \tau_e^{-1} [X^n],$$

where P_n is the volume production rate of X^n, $A_{n,1}$ the probability of the $n \rightarrow 1$ transition, k_i the deactivation coefficients and $\tau_e = \left(\sum_1 A_{n,1} + \sum_i k_i [M_i]\right)^{-1}$ is the effective lifetime. The volume emission rate $n \rightarrow m$ is thus given by:

$$\eta_{n,m} = [X^n] A_{n,m} = \frac{P_n}{B^{-1} + A_{n,m}^{-1} \sum_i k_i [M_i]}$$

where $B = \dfrac{A_{n,m}}{\sum_1 A_{n,1}}$ is the radiative branching ratio.

The effective lifetime at the peak of the emission rate profile may be considerably smaller than the radiative lifetime as will be shown below. Recent measurements (Deans and Shepherd 1978, Rees et al., 1977, Rusch and Gérard, 1980) have indicated

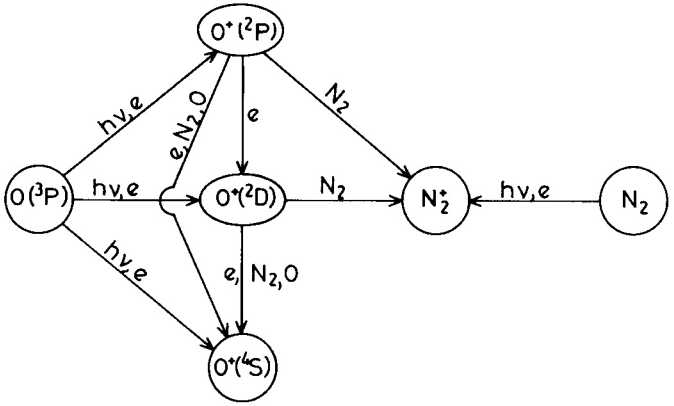

Figure 2 : Block diagram showing the role of $O^+(^2P)$ and $O^+(^2D)$ in the ionosphere.

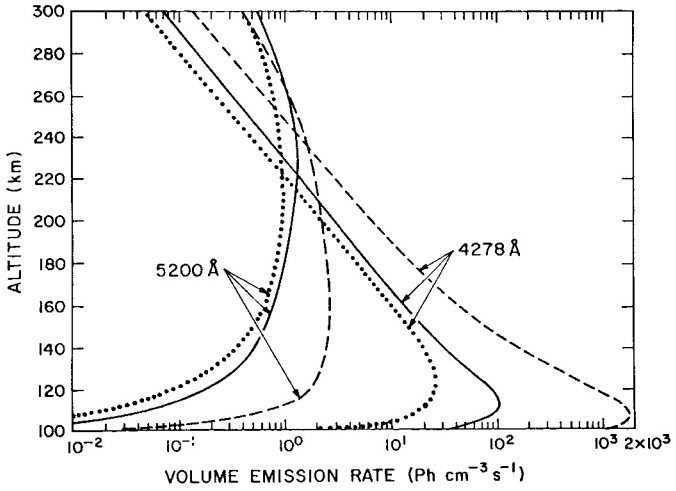

Figure 3 : Vertical distribution of the N_2^+ 4278 A and NI 5200 A emission rates for three different electron energy spectra (from Rusch and Gérard, 1980).

the quantum yield for $N(^2P)$ has not been measured. Zipf et al. 1980 have calculated the yield of $N(^4S)$, $N(^2D)$ and $N(^2P)$ atoms formed by the $N_2 + e \rightarrow N + N$ dissociation to be 0.46 : 0.35 : 0.19, respectively. The products of the $N(^2P) + O$ deactivation may be $N(^2D)$ or $N(^4S)$ atoms. If the former is created efficiently by this process, most of the $N(^2P)$ atoms are converted to $N(^2D)$ and a high effective quantum yield may be reached for $N(^2D)$, in agreement with mid and high latitude models of nitric oxide.

$N(^2D)$. A considerable interest for metastable $N(^2D)$ atoms arises from the role played by this species as a source of thermospheric nitric oxide. Its production mechanisms and sinks seem to be well understood due to the large body of data collected by the AE-C and D satellites for the $^4S - {}^2D$ transition at 5200 A. Figure 3 shows the odd nitrogen thermospheric cycle. $N(^2D)$ has three sources of magnitude roughly comparable to the N_2 ionization rate, which explains why, in spite of its extremely long radiative lifetime (26 hrs), this doublet easily reaches measurable emission rates. Quenching rates have been deduced from the analysis of the VAE dayglow measurements (Fredrick and Rusch, 1977). The latter value is about one order of magnitude larger than the laboratory determination by Davenport et al. (1976) when the probable increase of k_O with temperature is taken into accounts. Rusch and Gérard (1980) have recently examined on the basis of AE-D measurements whether this set of quenching coefficients and $N(^2D)$ quantum yields usually assumed for mid-latitude conditions also adequately explains the particle-excited nighttime 5200 A emission. They found that a reasonably good match is obtained with the observations using the following values of $N(^2D)$ efficiencies :

$$NO^+ + e \rightarrow N(^2D) + O , \qquad f_1 = 0.80$$

$$N_2 + e \rightarrow N + N(^2D) + e \qquad f_2 = 0.60$$

and $$N_2^+ + O \rightarrow NO^+ + N(^2D) , \qquad f_3 = 1.0$$

As mentioned above when the $N(^2P) + O$ deactivation is taken into account, the effective value of f_2 is nearly equal to 0.8 in this model. Figure 3 shows the calculated N_2^+ 4278 A and NI 5200 A volume emission rates for three different measured electron energy spectra. They show a broad peak of $N(^2D)$ roughly extending from 140 to 300 km and reaching about 1×10^5 cm^{-3}. The comparison between mid-latitude and high latitude sources is also of interest. When the production results from electron impact on N_2, the three sources listed above are of nearly equal magnitude, whereas at mid-latitudes the second one reaches only 10% of the total production. In the aurora, roughly four N atoms are created for each N_2 ionization and with

the efficiences adopted in this mode, the global efficiency for $N(^2D)$ production is 83%. Consequently, an empirical ratio of $\sim$ 3.3 $N(^2D)$ produced/N_2 ionization may be adopted. The wide range of altitudes where $N(^2D)$ atoms are found makes it unrealistic to define single effective lifetimes for this state but the large values of τ_e make it a very good candidate for horizontal transport by winds. This point will be illustrated in section 4.

$O(^1D)$. The OI ^3P - ^1D doublet at 6300 - 6363 A is by far the most prominent feature amongst the F-region emissions. Understanding of its altitude distribution and excitation mechanisms is essential since ground-based measurements of its intensity and Doppler shift are used extensively to determine the electron energy spectrum and the neutral winds respectively.

The classical sources of $O(^1D)$ due to particle precipitation are :

$$O(^3P) + e_{s,th} \rightarrow O(^1D) + e_{s,th}$$

and $$O_2^+ + e \rightarrow O + O(^1D) \ ,$$

where the electrons exciting $O(^3P)$ may be secondaries or fast thermal electrons and the quantum yield of $O(^1D)$ for dissociative recombination of O_2^+ is 0.66. This state is mainly quenched by N_2 (Hays et al. 1978).

This theory could hardly be tested against ground-based observations due to the diffuse character of the 6300 A morphology. However, analysis of a coordinated AE-rocket measurement over Fort-Churchill showed that another source of $O(^1D)$ was needed to explain the observed emission rate. Figure 4 shows the measurements as well as the $O(^1D)$ production rate by the two processes described above, where the curve marked "Harp" is the contribution of the first process calculated using the measured electron flux. The comparison clearly shows that an extra source of ^1D is needed to account for the observations. Rusch et al. (1978) have proposed that the energy transfer process :

$$N(^2D) + O \rightarrow NO + O(^1D) + 3.8 \text{ eV} \ ,$$

may be the missing source. They showed that the efficiency should be near 100% to explain the ^1D vertical profile. Laboratory spectra of the infrared emission from nitric oxide formed by this process show that the vibrational distribution of NO breaks up at v' = 7 which corresponds to the threshold of formation of $O(^1D)$ instead of $O(^3P)$. The close temporal correlation between the 5200 A and the 6300 A intensities observed during time variations is also in agreement with this hypothesis.

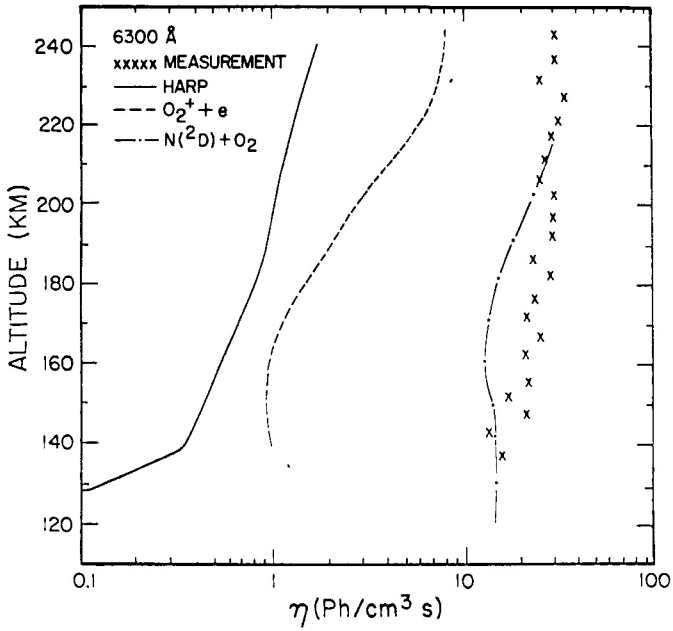

Figure 4 : Measured and calculated volume emission rates of $O(^1D)$ for various excitation processes (from Rusch et al. 1978).

Recently, efficiencies for the production of $O(^1D)$ by primary electrons in various energy channels have been deduced by Shepherd et al. (1980) by comparing the measured 6300 A emission rate with the ISIS II low energy electron spectrometer.

Table I summarizes our recommended set of values concerning the sources and quenching of the five important metastable states described above. The last two columns list the altitude of the peak and the calculated effective lifetime at these altitudes. These figures are only approximate since the altitude of the maximum is sometimes loosely defined and depends strongly on the primary electron spectrum.

4. REMOTE SENSING BY F-REGION OPTICAL EMISSIONS

The use of optical emissions as a remote sensing technique of the polar atmosphere and ionosphere has developed along three major axes :

Table 1 : F-region metastable atom sources and quenching

transition	λ(A)	sources	quantum yield	loss coefficients ($cm^3.s^{-1}$)	peak altitude (km)	effective lifetime (s)
[OI] $^3P - {}^1D$	6300-64	$O + e \rightarrow O(^1D) + e$ $O_2^+ + e \rightarrow O(^1D) + O$ $N(^2D) + O_2 \rightarrow O(^1D) + NO$	0.66	$A = 9.1 \times 10^{-3} s^{-1}$ $k_{N_2} = 3 \times 10^{-11}$	300	20
[OII] $^4S - {}^2P$ and $^2D - {}^2P$	2470 7320-30	$O + e \rightarrow O^+(^2P) + 2e$	0.22	$A = 0.22\ s^{-1}$ $k_O = 5.2 \times 10^{-11}$ $k_{N_2} = 4.8 \times 10^{-10}$ $k_e = 1.9 \times 10^{-7}(300/T_e)^{1/2}$	200	0.4
[OII] $^4S - {}^2D$	3729	$O + e \rightarrow O^+(^2D) + 2e$ $O^+(^2P) \rightarrow O^+(^2D) + h\nu$ $O^+(^2P) + M \rightarrow O^+(^2D) + M$	0.32	$A = 7.7 \times 10^{-5} s^{-1}$ $k_O < 1 \times 10^{-11}$ $k_{N_2} = 1 \times 10^{-10}$ $k_e = 1.5 \times 10^{-7}(300/T_e)^{1/2}$	300(?)	15
[NI] $^4S - {}^2P$ and $^2D - {}^2P$	3466 10,395-404	$N_2 + e \rightarrow N(^2P) + N + e$ $N_2^+ + e \rightarrow N(^2P) + N$ $(N_2^+)^* + O \rightarrow NO^+ + N(^2P)$	to 0.05 0.20 0.50	$A = 8.3 \times 10^{-2}\ s^{-1}$ $k_O = 1 \times 10^{-11}$ to 3×10^{-11} $k_{O_2} = 2.6 \times 10^{-12}$ $k_e = 4 \times 10^{-10}(300/T_e)^{-1/2}$	120	0.4
[NI] $^4S - {}^2D$	5199-5201	$N_2 + e \rightarrow N(^2D) + N^{(+)} + (2)e$ $NO^+ + e \rightarrow N(^2D) + O$ $N_2^+ + O \rightarrow NO^+ + N(^2D)$	0.75 0.8 1.0	$A = 1.1 \times 10^{-5}\ s^{-1}$ $k_O = 4 \times 10^{-13}$ $k_{O_2} = 6 \times 10^{-12}$ $k_e = 4 \times 10^{-10}(300/T_e)^{-1/2}$	250	1000

Table 1 : F-region metastable atom sources and quenching

transition	λ(A)	sources	quantum yield	loss coefficients ($cm^3.s^{-1}$)	peak altitude (km)	effective lifetime (s)
[OI] $^3P - {}^1D$	6300-64	$O + e \rightarrow O(^1D) + e$ $O_2^+ + e \rightarrow O(^1D) + O$ $N(^2D) + O_2 \rightarrow O(^1D) + NO$	0.66	$A = 9.1 \times 10^{-3} s^{-1}$ $k_{N_2} = 3 \times 10^{-11}$	300	20
[OII] $^4S - {}^2P$ and $^2D - {}^2P$	2470 7320-30	$O + e \rightarrow O^+(^2P) + 2e$	0.22	$A = 0.22\ s^{-1}$ $k_O = 5.2 \times 10^{-11}$ $k_{N_2} = 4.8 \times 10^{-10}$ $k_e = 1.9 \times 10^{-7}(300/T_e)^{1/2}$	200	0.4
[OII] $^4S - {}^2D$	3729	$O + e \rightarrow O^+(^2D) + 2e$ $O^+(^2P) \rightarrow O^+(^2D) + h\nu$ $O^+(^2P) + M \rightarrow O^+(^2D) + M$	0.32	$A = 7.7 \times 10^{-5} s^{-1}$ $k_O < 1 \times 10^{-11}$ $k_{N_2} = 1 \times 10^{-10}$ $k_e = 1.5 \times 10^{-7}(300/T_e)^{1/2}$	300(?)	15
[NI] $^4S - {}^2P$ and $^2D - {}^2P$	3466 10,395-404	$N_2 + e \rightarrow N(^2P) + N + e$ $N_2^+ + e \rightarrow N(^2P) + N$ $(N_2^+)^* + O \rightarrow NO^+ + N(^2P)$	to 0.05 0.20 0.50	$A = 8.3 \times 10^{-2}\ s^{-1}$ $k_O = 1 \times 10^{-11}$ to 3×10^{-11} $k_{O_2} = 2.6 \times 10^{-12}$ $k_e = 4 \times 10^{-10}(300/T_e)^{-1/2}$	120	0.4
[NI] $^4S - {}^2D$	5199-5201	$N_2 + e \rightarrow N(^2D) + N^{(+)} + (2)e$ $NO^+ + e \rightarrow N(^2D) + O$ $N_2^+ + O \rightarrow NO^+ + N(^2D)$	0.75 0.8 1.0	$A = 1.1 \times 10^{-5}\ s^{-1}$ $k_O = 4 \times 10^{-13}$ $k_{O_2} = 6 \times 10^{-12}$ $k_e = 4 \times 10^{-10}(300/T_e)^{-1/2}$	250	1000

i) determination of the characteristic energy of the precipitated electron energy.

ii) evaluation of composition changes caused by vertical upwelling due to local Joule heating.

iii) measurement of neutral winds and electromagnetic drifts by observation of the Doppler width and shift of F-region emissions. Developments of the three techniques are briefly described in the following paragraphs.

4.1. Determination of the precipitation characteristic energy

The emission rate ratio of a forbidden to an allowed emission may, once the excitation mechanisms are known quantitatively, be used to evaluate the spectral index of the flux of precipitated electrons. For example, Rees and Luckey (1974), assuming a maxwellian distribution of energies have calculated the 6300 A/4278 A ratio versus I(4278 A) for various values of the characteristic energy using the "classical" production mechanisms for $O(^1D)$. Conversely, the observed ratio and absolute 4278 A intensity may be used to determine the hardness of the precipitation. However, as mentioned in the previous section, a new source of $O(^1D)$ atoms needs to be added to the model and until revised tables including this extra production term are available (Rees, pers. comm.), the figures of Rees and Luckey should be used with caution.

4.2. Neutral composition changes

Observations of forbidden lines whose relative intensities are sensitive to the N_2(or O_2)/O ratio may be used to monitor the neutral composition in the polar thermosphere. For example, the (OII 7320 A)/(N_2^+ 4278 A) ratio is given by :

$$\frac{n(7320\ A)}{n(4278\ A)} = C \frac{[O]}{[N_2]} \quad Q \quad ,$$

where Q is the quenching factor described in section 2. Consequantly, this ratio may be used to determine changes of the O/N_2 ratio due to vertical upwelling generated by Joule heating.

4.3. Wind and drift measurements

The technique using the 6300 A line shift and Doppler width measurements to determine F-region winds has been used extensively and will be employed for the first time on a satellite in the Dynamics Explorer mission. The method and new results

for the polar regions are described by Smith (this volume) and will not be repeated here. Although it has never been tested, progress in sensitivity of Fabry-Perot and Michelson interferometers should permit the method to be extended to weaker features such as NI 5200 A.

It is clear that morphology of metastable emission can be greatly influenced by the presence of horizontal neutral winds. Table I shows that effective lifetimes may reach several seconds near the peak of the emission profile. To illustrate this point, figures 5 and 6 show the effect on the morphology of the $N(^2D)$ distribution of a horizontal wind blowing through an auroral arc. The particle precipitation is similar to that used by Roble and Gary (1979). The altitude dependence of the wind velocity is given by :

$$v(z) = 50 + 0.75(Z - 75) \quad m/S.$$

The contours are shown in units of $\log(N^2D)$ in figure 5, 15 and 60 min after the wind is turned on. A downwind plume of metastable atoms is formed, similar to the result for NO described by Roble and Gary. Consequently, the 5200 A intensity is enhanced by a large factor on the downwind side of the arc. The particle flux is turned off after 60 min and figure 6 illustrates the morphology at t = 75 min and 90 min. The enhanced region of $N(^2D)$ gradually disappears under the effects of the wind and quenching by O and O_2. Evidence for such transport effects was presented by Shepherd et al. (1970) and Frederick and Hays (1978).

Measurements of Doppler shifts of emissions from metastable ions such as $O^+(^2P)$ have also been used to determine ion drift velocities in the high latitude thermosphere. Preliminary observations were reported by Meriwether et al. (1974) but with the improved sensitivity of recent instruments, better accuracies could be obtained and this technique should receive greater attention in the future.

Finally, another optical technique for remotely sensing drift velocities has been suggested by Haerendel (1976). A balloon-borne all-sky camera is used to observe the resonance scattering of sunlight by Mg^+ ions at 2800 A. These ions are produced in the E-region by meteor ablation and transported upwards by winds and drifts. Their presence was observed optically in the F-region by Gérard (1976) and by Grebowsky and Brinton (1978) using a mass spectrometer. Striations similar to those observed after Ba rocket releases should be observed in the presence of field-aligned currents.

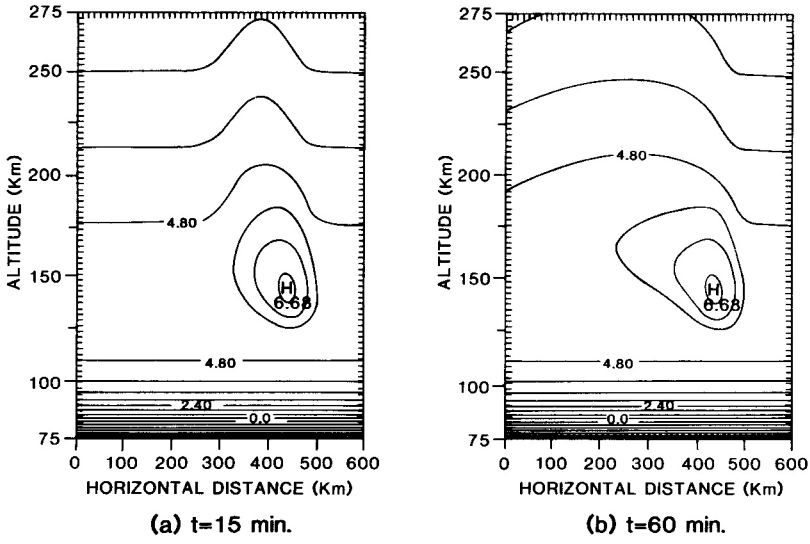

Figure 5 : Contour plots of $\log_{10}(N^2D)$ for an auroral arc with neutral wind. Contours are separated by 0.6 unit. (Courtesy of R.G. Roble).

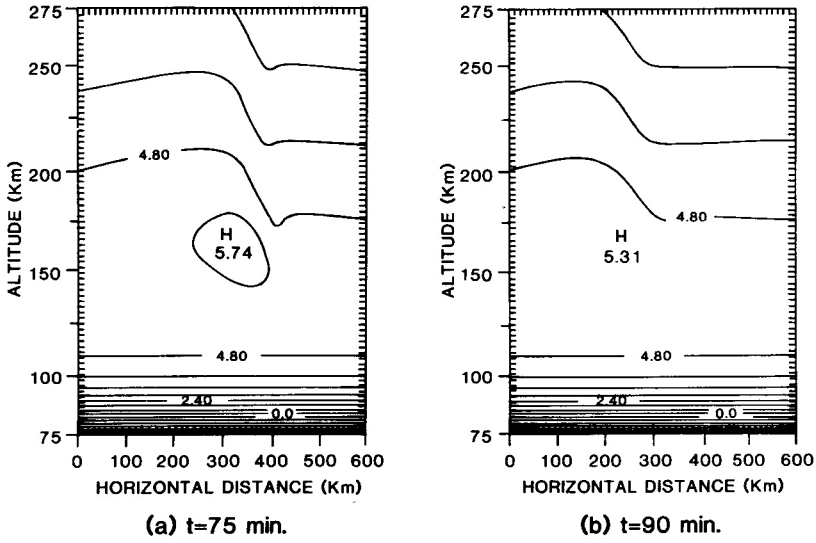

Figure 6 : Same as figure 5, except that the source has been turned off at t = 60 min.

ACKNOWLEDGMENTS

The author is supported by the Belgian Foundation for Scientific Research (FNRS).

REFERENCES

Dalgarno A.L., and Lejeune G. 1971, Planet. Space Sci., 19, 1653.
Davenport J.E., Slanger T.E., and Black G. 1976, J. Geophys. Res. 81, 12.
Deans A.J., and Shepherd G.G. 1978, Planet. Space Sci., 26, 319.
Frederick J.E., and Rusch D.W. 1977, J. Geophys. Res., 82, 3509.
Frederick J.E., and Hays, P.B. 1978, Planet. Space Sci., 26, 339.
Gérard J.C. 1976, J. Geophys. Res., 81, 83.
Gérard J.C., and Harang O.E. 1980, J. Geophys. Res., 85 Accepted for publication.
Grebowsky J.M., and Brinton H.C., 1978, Geophys. Res. Lett., 5 791.
Haerendel G. 1976, Proceeding ESA Symposium, ESA/SP115.
Hays, P.B., Carignan G., Kennedy B.C., Shepherd G.G., and Walker J.C.G. 1973, Radio Sci., 8, 369.
Hays P.B., Rusch D.W., Roble R.G., and Walker J.C.G. 1978, Rev. Geophys. Space Phys., 16, 225.
Henry R.J., Burke P.G., and Sinfailam A.L. 1969, Phys. Rev., 178, 218.
Meriwether J.W., Hays P.B., McWatters H.D., and Nagy A.F.V. 1974, Planet. Space Sci., 22, 636.
Rees M.H. 1975, Planet. Space Sci., 23, 1589
Rees M.H., and Luckey D. 1974, J. Geophys. Res., 79, 5181.
Rees M.H., Stewart A.I., Sharp W.E., Hays, P.B., Hoffman R.A., Brace L.H., Doering J.P., and Peterson W.K. 1977, J. Geophys. Res., 82, 2250.
Roble R.G. 1975, Planet. Space Sci., 23, 1017.
Roble R.G., and Gary J.M. 1979, Geophys. Res. Lett., 6, 703.
Rusch D.W., Torr D.G., Hays P.B., and Walker J.C.G. 1977, J. Geophys. Res., 82, 719
Rusch D.W., Gérard J.C., and Sharp W.E. 1978, Geophys. Res. Lett., 5, 1043.
Rusch D.W., and Gérard J.C. 1980, J. Geophys. Res., 85, 1285.
Shepherd G.G., Pieau J.F., Creuzberg F., McNamara A.G., Gérard J.C., McEwen D.J., Delana B., and Whitteker J.H. 1976, Geophys. Res. Lett., 3, 69.
Shepherd G.G., Winningham J.D., Bunn F.E., and Thirkettle K.W. 1980, J. Geophys. Res., 85, 715.
Torr D.G., and Torr M.R. 1980, J. Geophys. Res., 85, 783.
Vallance-Jones A., and Gattinger R.L. 1975, Can. J. Phys., 53 1806.
Young R.A., and Dunn O.J. 1975, J. Chem. Phys., 63, 1150.
Zipf E.C., Espy P.J., and Boyle C.F. 1980, J. Geophys. Res., 85, 687.